

NUMERICAL ANALYSIS OF PRE- AND POST-HEATING STRATEGIES FOR REDUCING RESIDUAL STRESSES IN LASER-BASED DIRECTED ENERGY DEPOSITION

Usman Tariq ^a, Sung-Heng Wu ^a, Muhammad Arif Mahmood ^b, Frank Liou ^a

^a Department of Mechanical and Aerospace Engineering, Missouri University of Science
and Technology, Rolla, MO 65409, USA

^b Intelligent Systems Center, Missouri University of Science and Technology, Rolla, MO 65409,
USA

Abstract

This research explores how pre- and post-heating methods influence temperature gradients and residual stresses in Ti-6Al-4V components produced via Laser Directed Energy Deposition (DED). Using numerical simulations complemented by experimental validation, the study assesses two heating intensities—40% (low) and 80% (high)—relative to the main deposition laser power. Results demonstrate that pre-heating substantially decreases thermal gradients, thereby effectively reducing residual stresses within the deposited structure. Conversely, post-heating exhibited only minor changes in local temperature fields, with comparatively limited effects on overall stress mitigation. These outcomes underline that managing initial thermal conditions through pre-heating strategies is critical for effectively controlling residual stresses in additive manufacturing processes. The study provides insights into optimizing thermal management protocols to enhance the mechanical integrity of laser-based DED components.

Keywords: Additive Manufacturing; DED; Pre-heating; Post-heating; Residual stresses.

Introduction

DED is an advanced additive manufacturing (AM) technique that enables the fabrication and repair of metallic components by precisely depositing material layer by layer using a high-energy heat source, such as a laser or electron beam, in combination with metal powder or wire feedstock [1]. This process offers advantages such as high deposition rates, material efficiency, and the ability to build large-scale components with complex geometries [2]. However, a significant challenge in DED is the development of residual stresses (RS), which arise due to rapid heating and cooling cycles during deposition [3]. These stresses can lead to part distortion, cracking, and mechanical property degradation, ultimately affecting the reliability of DED-manufactured components.

To address the issue of residual stresses, researchers have extensively investigated various mitigation strategies. Experimental techniques such as X-ray diffraction and digital image correlation have been used to validate numerical simulations of stress evolution [4]. Finite element modeling (FEM) has been widely utilized to predict the thermal and mechanical responses during deposition [5]. Several studies have explored the role of scan strategies, including bidirectional and unidirectional paths, in controlling thermal gradients and reducing stress accumulation [6].

Additionally, the optimization of laser parameters, such as power, scan speed, and hatch spacing, has been shown to influence residual stress distributions [7].

Beyond scan path optimization, researchers have examined interlayer dwell times as a potential stress-relief approach, allowing for controlled cooling between layers [8]. Some studies have investigated substrate pre-heating as a means of reducing thermal gradients, thus lowering residual stress magnitudes [7], [3]. While these methods contribute to stress mitigation, they often have trade-offs in terms of process efficiency and part microstructure stability. Notably, the impact of “post-heating strategies” has received limited attention in DED research, even though controlled post-heating could facilitate stress relaxation.

This study employs both experimental and numerical approaches to investigate the influence of pre-heating and post-heating strategies on residual stress evolution in DED. Experimentally, a laser DED system equipped with thermocouples is used to capture real-time temperature data. Concurrently, a finite element model is developed to simulate transient thermal and mechanical behavior. The objectives of this study are to evaluate the effectiveness of pre-heating and post-heating strategies in reducing residual stress magnitudes, analyze their impact on thermal profiles, and compare stress distributions across different heating conditions. The findings provide valuable insights for optimizing DED process parameters to enhance the structural integrity of additively manufactured components.

Numerical Model of DED

A comprehensive three-dimensional thermo-mechanical numerical model was developed for this study, simulating the DED process specifically for Titanium alloy (Ti6Al4V) as shown in Figure. 2. The simulation framework consisted of two sequential phases: a transient thermal analysis to calculate temperature distributions, followed by a mechanical analysis to predict residual stresses and deformations. The model was implemented using the FEM software Abaqus. Furthermore, to adequately resolve the steep thermal gradients near the moving heat source, we refined the mesh such that the laser beam (or melt-pool) width spans at least 4–5 elements in the track adjacent zone, a common practice in additive FE simulations that employ localized refinement around the heat source [8].

1. Thermal Model

In DED, the evolution of stresses and resultant distortion heavily depends on the thermal profile, whereas mechanical deformation minimally impacts the thermal profile. Hence, thermal analysis was conducted separately from mechanical effects. An 8-node linear brick element type (DC3D8) was selected for discretization. The transient heat conduction within the domain was solved using the three-dimensional heat conduction equation:

$$\frac{\partial}{\partial x} \left(k \frac{\partial T}{\partial x} \right) + \frac{\partial}{\partial y} \left(k \frac{\partial T}{\partial y} \right) + \frac{\partial}{\partial z} \left(k \frac{\partial T}{\partial z} \right) + Q_{int} = \rho C_p \frac{\partial T}{\partial t} \quad (1)$$

where T is the temperature (°C), ρ is the material density (kg/m³), C_p is the specific heat capacity (J/kgK), k is the thermal conductivity (W/mK), and Q_{int} represents the internal heat generation per unit volume (W/m³), primarily due to laser energy absorption. A volumetric heat source model,

specifically Goldak's double-ellipsoidal model, is employed to represent laser-material interaction:

$$Q = \frac{6\sqrt{3}P\eta}{abc\sqrt{\pi}} \exp\left(-\frac{3x^2}{a^2} - \frac{3y^2}{b^2} - \frac{3(z - V_s t)^2}{c^2}\right) \quad (2)$$

where P is laser power (W), η is absorption efficiency, a (2.2), b (1.1) and c (1.1) represent heat source dimensions (mm), and V_s is the scanning velocity (m/s). To simulate thermal losses, convective heat losses to the environment were modeled by applying Newton's cooling law:

$$q_{conv} = h_c(T - T_{amb}) \quad (3)$$

where h_c is the convective heat transfer coefficient 35 (W/m²K), T is the local surface temperature, and T_∞ is the ambient temperature. Radiative heat losses were modeled using the Stefan-Boltzmann law:

$$q_r = \varepsilon\sigma(T^4 - T_{env}^4) \quad (4)$$

where ε is emissivity with 0.8, σ is the Stefan-Boltzmann constant (5.67×10^{-8} W/m²K⁴).

2. Mechanical Model

The mechanical response of the deposited material is governed by the equilibrium equation:

$$\nabla \cdot \sigma + b = 0 \quad (5)$$

where σ represents the Cauchy stress tensor (Pa) and b is the body force vector (N/m³). The total strain tensor is decomposed as follows:

$$\varepsilon = \varepsilon^{elastic} + \varepsilon^{plastic} + \varepsilon^{thermal} \quad (6)$$

Where $\varepsilon^{elastic}$ corresponds to elastic deformation, $\varepsilon^{plastic}$ accounts for plastic deformation, and $\varepsilon^{thermal}$ represents thermal expansion/contraction using temperature dependent properties. Thermal strain is modeled as:

$$\varepsilon^{thermal} = \alpha(T - T_0)I \quad (7)$$

where α is the thermal expansion coefficient (1/K), T_0 is the reference temperature (room temperature), and I is the identity matrix. Stress-strain behavior follows Hooke's law for isotropic elasticity:

$$\sigma = C:\varepsilon^{elastic} \quad (8)$$

where C is the fourth-order elasticity tensor.

Materials and Methodology

1. Material Properties

The material selected for this numerical investigation is the widely used aerospace-grade Titanium alloy, Ti6Al4V. This alloy is particularly favored for AM processes such as DED due to its superior mechanical properties and compatibility with AM techniques. Ti6Al4V exhibits an exceptional combination of high strength-to-weight ratio, robust corrosion resistance, and reliable biocompatibility, making it an ideal candidate for aerospace, automotive, and biomedical applications. Accurate thermal-mechanical simulations of the DED process necessitate temperature-dependent material properties to precisely predict thermal behavior, stress evolution, and resultant deformations. Consequently, temperature-dependent physical and mechanical properties for Ti6Al4V were utilized in this numerical analysis and were taken from [9]. These

comprehensive and temperature-specific property data facilitate robust and realistic simulations, allowing precise capture of the alloy's complex behavior during the high-temperature cycles typical of the DED process.

2. Experimental Setup

Experimental validation of the numerical model was performed using a custom-built Laser DED system. This system featured an Nd:YAG laser capable of delivering a maximum power output of 1 kW. Metal powder was fed into the melt pool via an off-axis powder-feeding mechanism integrated with an inert gas shielding system to prevent oxidation and contamination during the deposition process. The experimental setup and in-house developed DED machine is shown in Figure. 1.

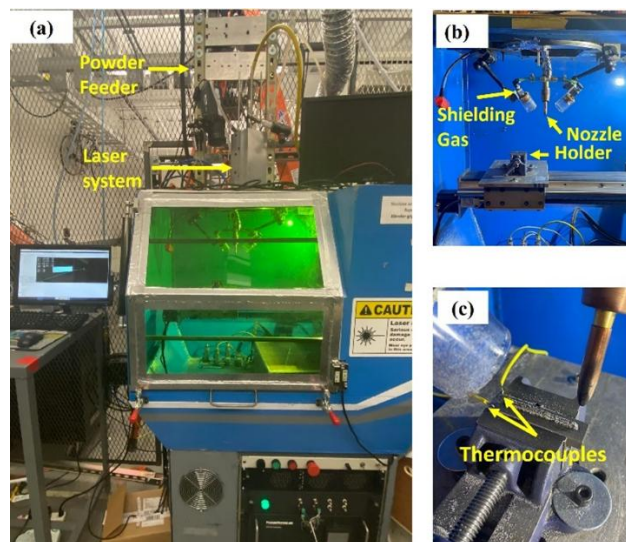


Figure 1. Experimental setup used for the laser DED process, showing (a) the overall DED system equipped with a 1 kW Nd:YAG laser and powder feeding system, (b) close-up view of the off-axis powder-feeding nozzle assembly and shielding gas arrangement, and (c) placement of two K-type thermocouples on the substrate to capture thermal histories during deposition.

For capturing accurate thermal histories during deposition, two K-type thermocouples were securely attached to the substrate surface. These thermocouples provided continuous temperature measurements, which were crucial for validating the accuracy and reliability of the numerical thermal predictions. The detailed build conditions employed in this experimental validation included: (a) Laser Power: 350 W, (b) Powder Feed Rate: 2.0 g/min, (c) Scanning Speed: 200 mm/min, (d) Laser Spot Size: 2.2 mm, employing a Gaussian energy distribution profile, and (e) Dwell Time per Track: 0.15 s.

3. Pre-and Post-heat Strategy

To systematically investigate the effectiveness of thermal management strategies in minimizing residual stresses, a set of numerical simulations was performed incorporating controlled pre- and post-heating techniques. These strategies were evaluated only after the successful experimental validation of the thermal model, ensuring accuracy and reliability of the

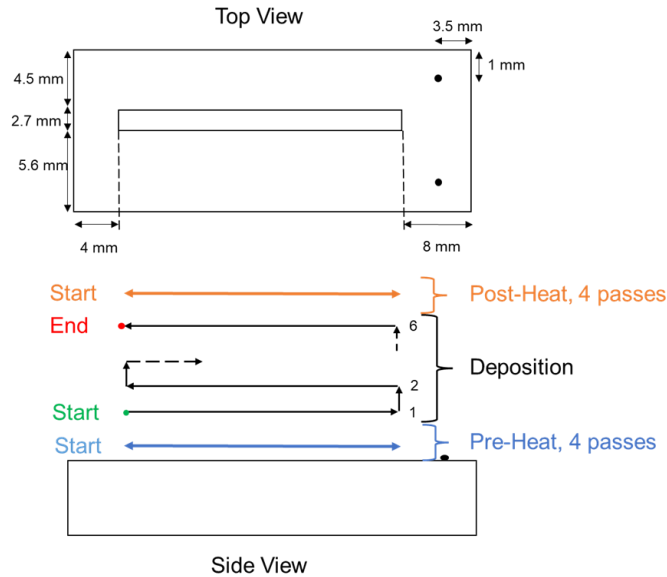


Figure 3. Pre- and post-heating scanning strategy used in numerical simulations (after thermal validation), demonstrating four consecutive passes for each heating scenario.

Results and Discussion

1. Thermal Validation

The accuracy of the numerical thermal model was verified by comparing the predicted temperature profiles during the deposition process with experimental measurements. Figure. 4 illustrates the numerically predicted temperature distribution using the conventional heating method during deposition. It shows a localized high-temperature region at the deposition location, confirming the simulation's ability to capture realistic thermal gradients necessary for proper material fusion and bonding. Additionally, Figure. 5 provides a quantitative comparison between the simulated temperatures and experimental data recorded by two K-type thermocouples (TC1 and TC2) placed on the substrate. Good agreement between simulation and experimental data is evident. Thermocouple 1 (TC1), positioned closer to the deposition track, recorded higher temperatures compared to Thermocouple 2 (TC2). This observation aligns with expectations, as proximity to the deposition region enhances conductive heat transfer efficiency, resulting in higher local temperatures. These comparisons between numerical and experimental results substantiate the accuracy and reliability of the thermal simulation, allowing subsequent mechanical analyses to confidently incorporate these validated thermal conditions.

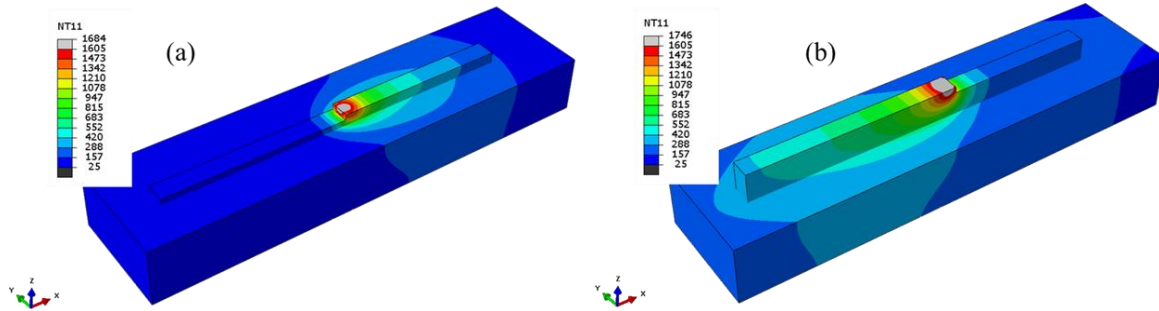


Figure 4. Simulated temperature distribution during laser deposition using conventional method, indicating localized heating at deposition area.

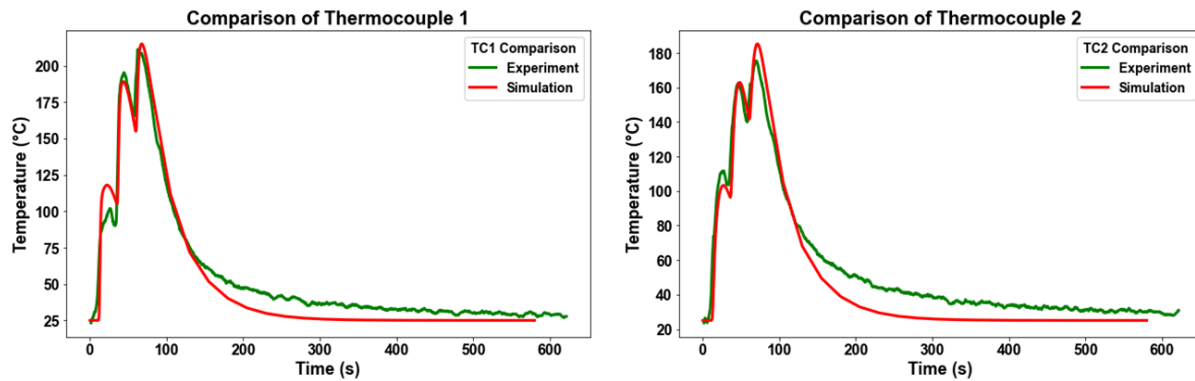


Figure 5. Numerical versus experimental thermocouple temperature comparison, showing agreement for TC1 and TC2.

2. No Pre-heating or Post-heating

Making a reference line as shown in Figure. 6 which at the top of the substrate where the deposit will be placed can be seen and used as a reference for this study. Figure. 7 illustrates the temperature distribution and corresponding von Mises stress profile for the baseline scenario (Case-00), where neither pre-heating nor post-heating was employed. Two distinct temperature profiles captured at the deposition start (blue line) and at the deposition end (orange line) are depicted. At the deposition start, the substrate temperature, as expected, remains near room temperature (25 °C). At the deposition endpoint (red vertical dashed line), the highest temperature (700 °C) is observed at the beginning of the deposited track. This peak temperature location correlates precisely with the initial point of deposition, attributable to the zig-zag scanning strategy employed, which accumulates heat at the initial deposition spot. The corresponding von Mises stress profiles at two conditions—immediately after deposition (end) and after unclamping—provide further insights. Initially, at the completion of deposition, von Mises stresses exhibit relatively lower values near the endpoint, despite the local high temperature. This phenomenon occurs because the material at this stage is still at elevated temperatures and thus not fully solidified, preventing the buildup of significant residual stresses. Conversely, at locations further from the endpoint, lower temperatures facilitate quicker solidification, leading to higher stress accumulation.

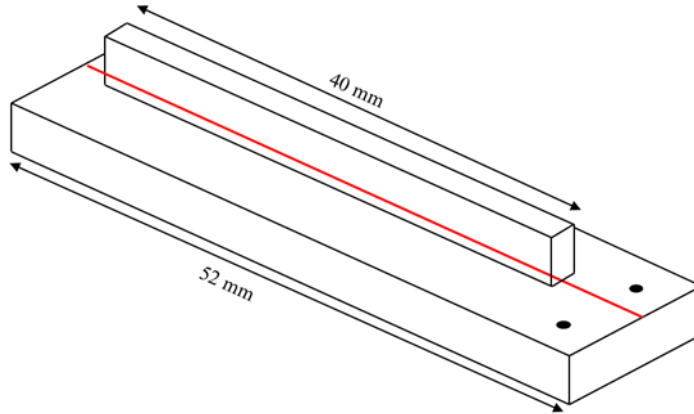


Figure 6. Reference line to make comparison of various pre-heating strategies.

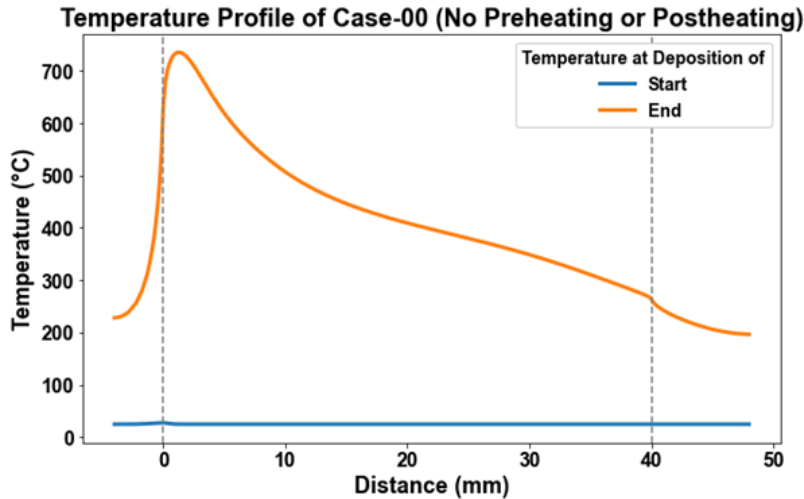


Figure 7. Temperature Profile of with no pre-heating or post-heating at the start and end of deposit.

Upon unclamping, the stress distribution significantly evolves, as shown in Figure. 8. Von Mises stresses increase markedly near the deposition endpoint, illustrating the formation of residual stresses as the deposited material cools down, contracts, and fully solidifies. This observed increase underscores the critical interplay between thermal gradients, cooling rates, and mechanical constraints in the formation and evolution of residual stresses during the DED process. These results highlight that the absence of pre-heating or post-heating treatments results in pronounced thermal gradients, triggering complex residual stress distributions. Notably, stress development is highly dependent on the thermal history, as demonstrated by the sharp increase in stresses after unclamping due to the elimination of mechanical constraints and complete solidification.

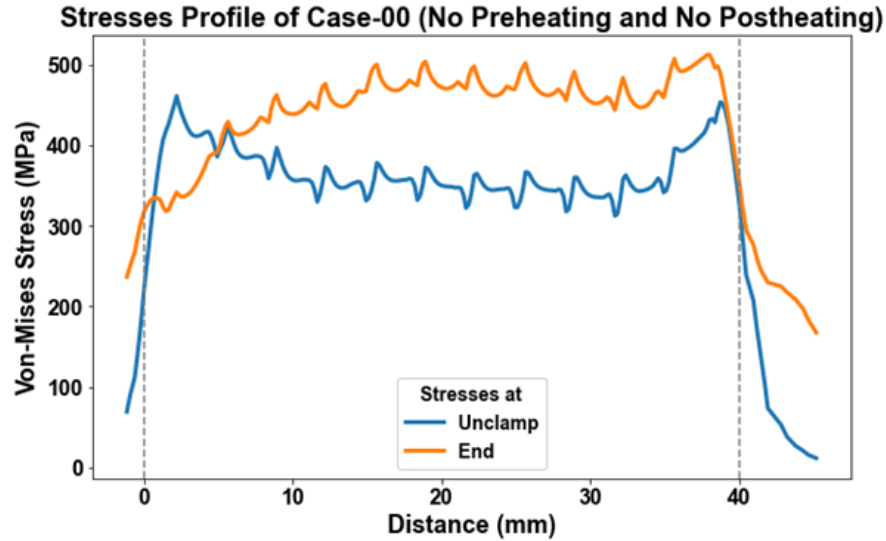


Figure 8. Von-Misses stresses profile with respect of temperature profile (top) at the end and unclamp condition.

3. Low and High Pre-heating

Figure. 9 demonstrates the results for the low pre-heating scenario (Case-10). As expected, the initial substrate temperature at the start of deposition is higher compared to Case-00, reaching approximately 200 °C, as indicated by the temperature profile. This initial elevation in temperature reduces the temperature gradient during deposition, leading to significantly lower von Mises stresses at the deposition start position (200 MPa) compared to Case-00 (325 MPa) as shown in Figure. 10. This observation confirms the effectiveness of pre-heating in mitigating initial residual stress formation.

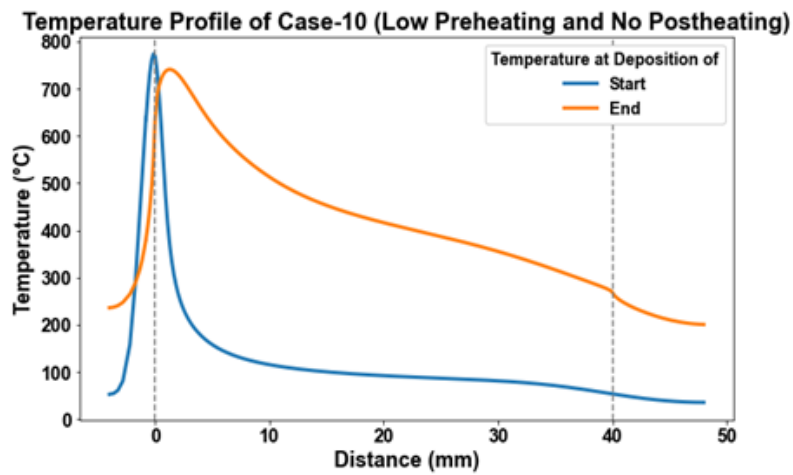


Figure 9. Temperature Profile of with low (40%) pre-heating and no post heating at the start and end of deposit.

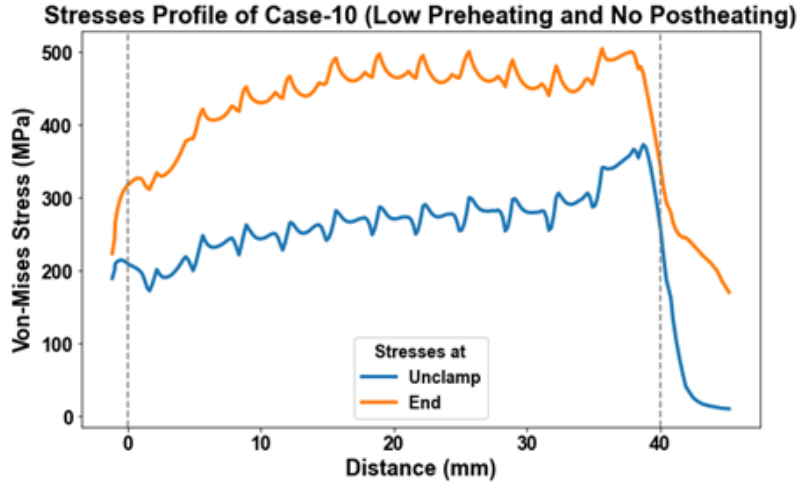


Figure 10. Von-Misses stresses profile with respect to temperature profile (top) at the end and unclamp condition.

A similar yet more pronounced trend is observed in Figure. 11 for the higher pre-heating condition (Case-20). Here, substrate temperature at deposition start further increases, reducing thermal gradients even more effectively. Correspondingly, von Mises stresses recorded at the deposition end condition are lower than both Case-00 and Case-10. The reduced stresses are directly attributable to the minimized temperature gradients achieved through higher pre-heating levels as shown in Figure. 12. It is important to note that towards the right side of the deposition track, the substrate and deposited material temperatures converge back to near room temperature. The larger temperature difference on this side results in elevated von Mises stresses. Conversely, near the start (left end), due to sustained higher substrate temperatures from pre-heating, stresses are notably lower. This confirms that higher initial substrate temperatures reduce the local thermal gradient and the subsequent residual stress development.

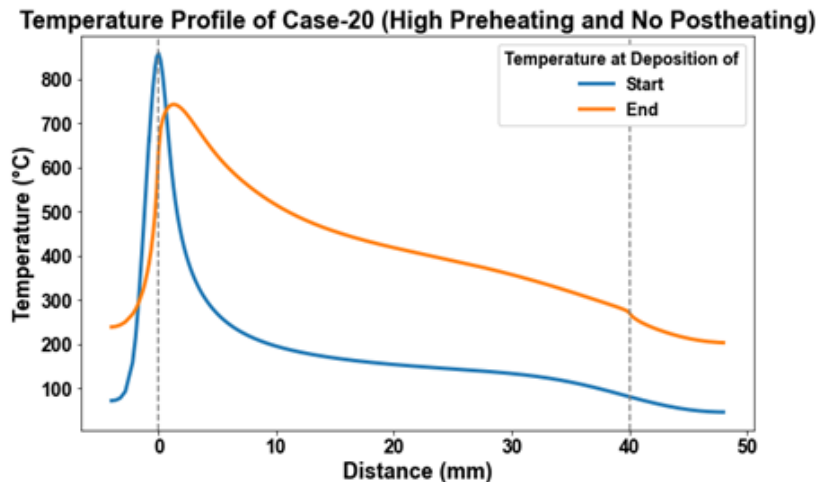


Figure 11. Temperature Profile of with low (80%) pre-heating and no post heating at the start and end of deposit.

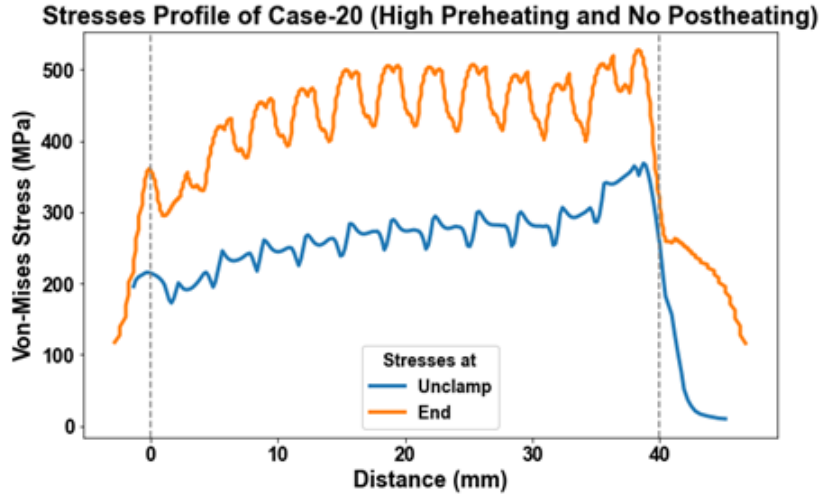


Figure 12. Von-Misses stresses profile with respect to temperature profile (top) at the end and unclamp condition.

To further elucidate the effects of pre-heating on temperature gradients and the resultant residual stress distribution, a comparative analysis of scenarios involving no pre-heating (Case-00), low-level pre-heating (Case-10, 40%), and high-level pre-heating (Case-20, 80%) was conducted, as illustrated in Figure. 13. It can be clearly observed from the temperature profiles that higher levels of pre-heating significantly reduce thermal gradients. The scenario without pre-heating (Case-00) exhibits a substantial temperature difference between the initial deposition zone and the substrate, resulting in pronounced stress accumulation upon cooling and unclamping. Conversely, the introduction of pre-heating at 40% (Case-10) and 80% (Case-20) notably elevates initial substrate temperatures, thereby effectively minimizing the thermal gradient between the deposited layer and substrate.

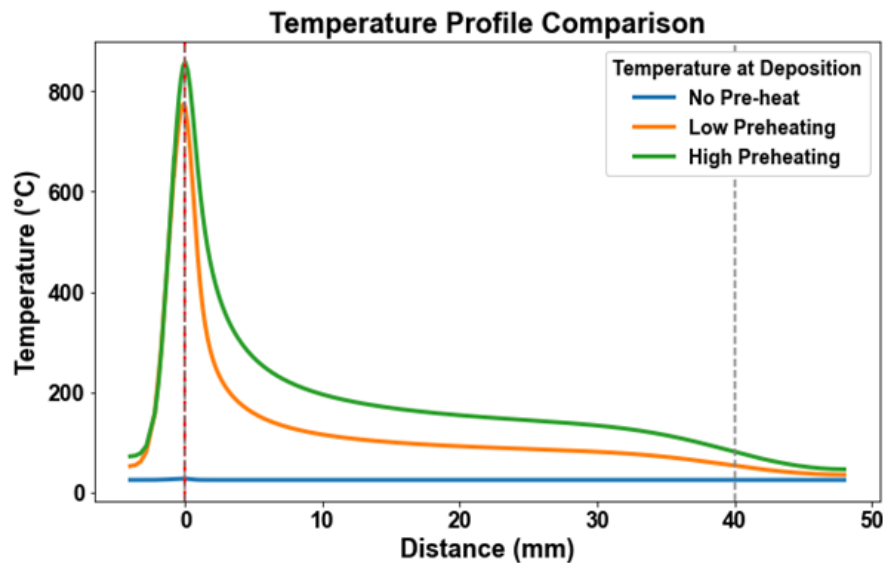


Figure 13. Comparison of temperature profiles for no pre-heating, low pre-heating (40%), and high pre-heating (80%) scenarios.

The corresponding von Mises stress distributions clearly support these observations. As shown in Figure. 14, von Mises stresses drastically decrease with increasing pre-heating intensity. The highest stresses are evident in the no-preheat case, where rapid cooling and significant temperature drops contribute to greater residual stress buildup. However, for the low and high pre-heating cases, stress levels are substantially lower, reflecting the reduced thermal gradients established by pre-heating. This behavior can be attributed to the fundamental relationship between thermal gradients and residual stress formation. Regions experiencing larger temperature variations during cooling solidify more rapidly and thus contract significantly, creating higher internal stresses. The pre-heated conditions mitigate these sharp thermal gradients, moderating cooling rates and thus directly reducing residual stress magnitudes. These observations clearly emphasize the effectiveness of pre-heating strategies in controlling residual stresses through the manipulation of temperature distributions during the DED process.

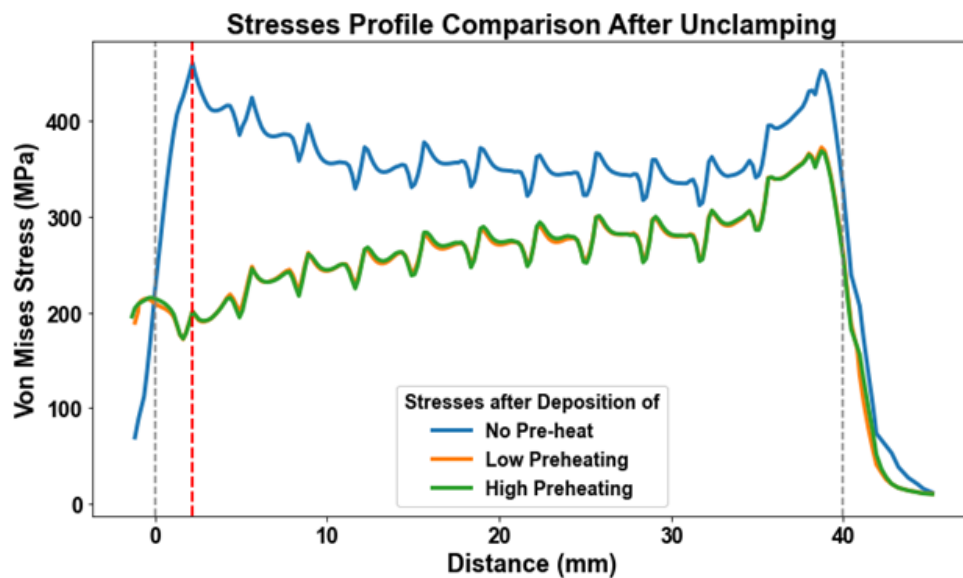


Figure 14. Comparison of von Mises stress profiles for no pre-heating, low pre-heating (40%), and high pre-heating (80%) scenarios.

4. Low and High Post-heating

The effects of the absence of post-heating (Case-00) on temperature distribution and resulting von Mises stresses over time are shown below. The red dashed reference line indicates the deposition length (40 mm), clearly differentiating the substrate region from the deposited material as shown in Figure. 15.

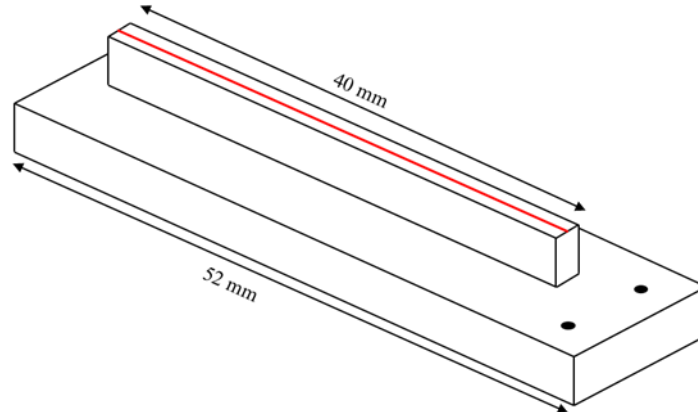


Figure 15. Reference line used for observing temperature and Von Mises stresses for post-heat analysis.

For no post-heating, immediately after deposition (0 sec), the peak temperature at the deposition start point reaches approximately 1800 °C, significantly above the melting temperature, which ensures proper fusion. Correspondingly, at this very instant, von Mises stresses are relatively low since the material is still molten and has yet to solidify, limiting stress buildup at this stage. However, as cooling progresses over subsequent time intervals (2 sec, 5 sec, 10 sec, 15 sec, and end of cooling), the temperature profile rapidly declines due to heat conduction into the substrate and convective losses to the environment as shown in Figure. 16. This rapid cooling induces substantial temperature gradients, which result in the progressive buildup of von Mises stresses due to solidification and associated thermal contraction Figure. 17. A notable observation in the stress profiles is the continual increase of residual stresses until the completion of the cooling stage, with stresses reaching their maximum magnitudes at this point. Furthermore, upon unclamping, slight stress relief is observed at both ends of the deposited specimen, indicating some elastic recovery when the external mechanical constraints are removed. These findings underscore the significance of temperature gradients and their direct influence on residual stress development during the DED process, particularly when no post-heating strategies are applied.

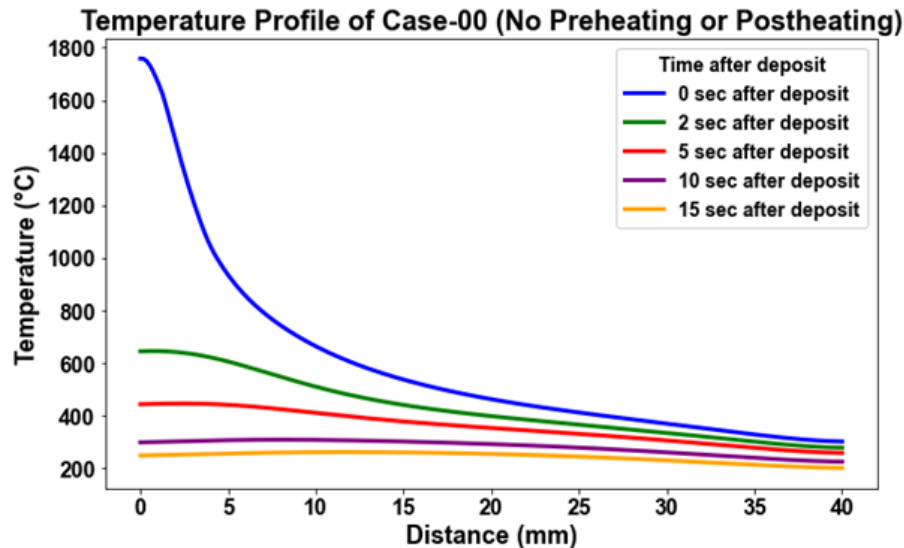


Figure 16. Temporal evolution of temperature for Case-00 without post-heating.

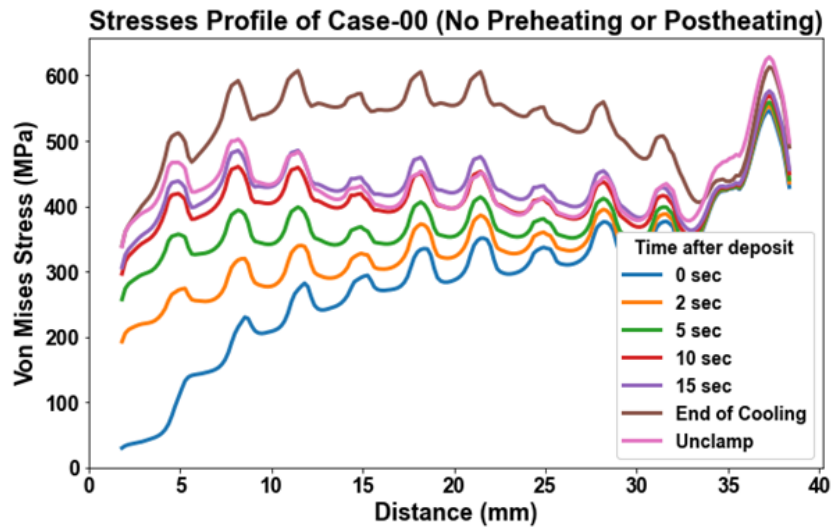


Figure 17. Temporal evolution of corresponding von Mises stresses for Case-00 without post-heating. Stress buildup over time is directly associated with rapid cooling and solidification-induced thermal contraction.

The effect of applying low-level post-heating (40%) without pre-heating (Case-01) is illustrated comprehensively below. Immediately following the deposition (0 sec), the temperature distribution exhibits a sharp peak around 1800 °C at the deposition start point, as expected. The subsequent low-intensity post-heating, designed to moderate the cooling rate and reduce temperature gradients, is clearly visible in the temperature profile. The repeated fluctuations observed in the temperature profiles on both ends correspond directly to the four scanning passes of the laser during the post-heating stage, causing transient localized reheating at these regions as shown in Figure. 18.

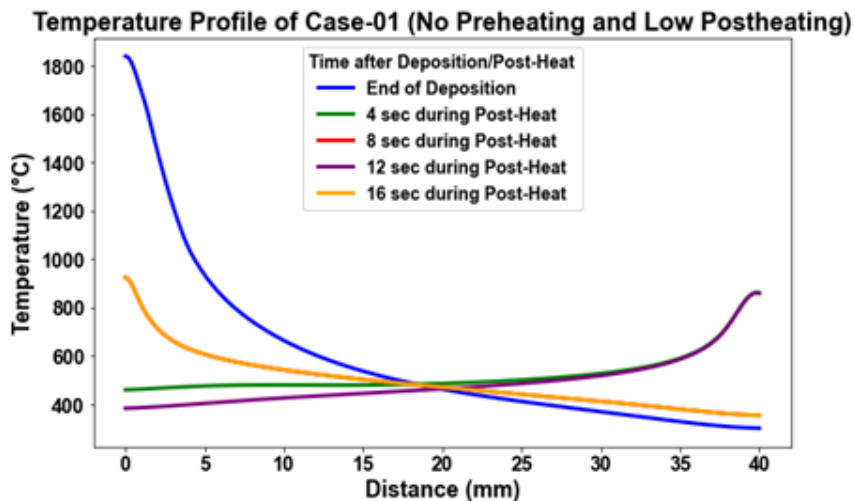


Figure 18. Temperature evolution during low-level (40%) post-heating without pre-heating (Case-01).

The corresponding von Mises stress profile also demonstrates distinct fluctuations correlating precisely to these repeated laser passes. Each pass of the laser temporarily reduces residual stresses at the specific heating locations due to localized temperature elevation, allowing minor stress relaxation through reduced thermal gradients as shown in Figure. 19. After the post-heating concludes, the temperature gradually declines uniformly across the specimen, leading to a slight increase and stabilization of von Mises stresses as shown in Figures. 20 and 21. Notably, compared to the scenario without post-heating, the stresses observed here are noticeably more uniform, although no substantial overall stress reduction is observed.

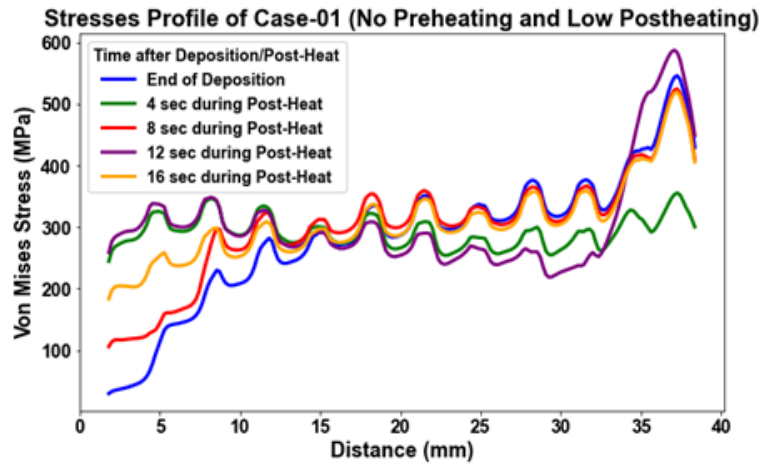


Figure 19. Von-misses evolution during low-level (40%) post-heating without pre-heating (Case-01).

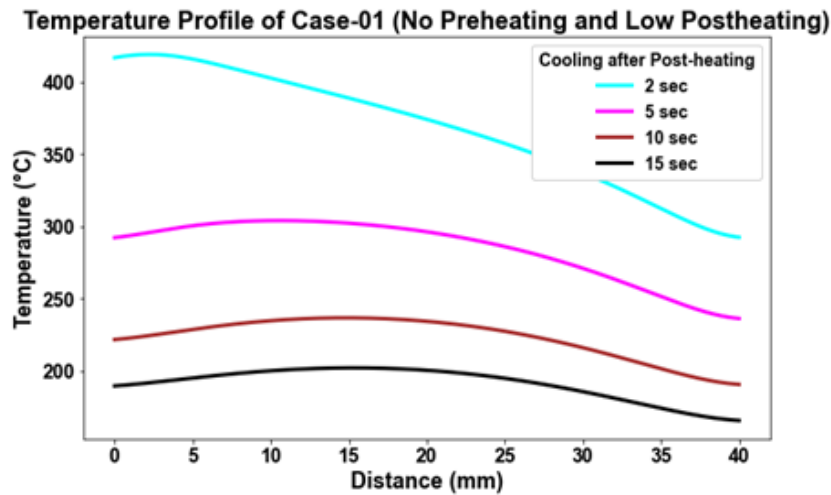


Figure 20. Temperature evolution after low-level (40%) post-heating without pre-heating (Case-01).

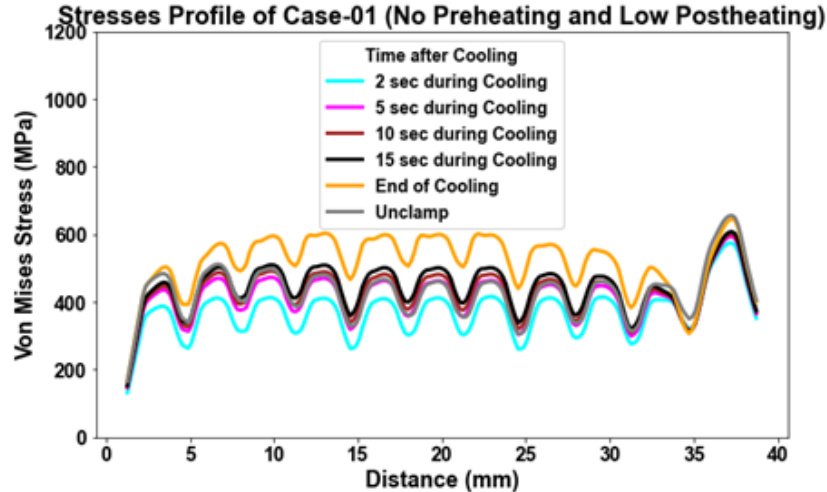


Figure 21. Von-misses evolution after low-level (40%) post-heating without pre-heating (Case-01).

Finally, upon unclamping, a clear but moderate reduction in stresses can be observed, attributed to the removal of mechanical constraints, allowing the specimen to elastically relax and partially alleviate residual stress. Thus, low-level post-heating contributes significantly towards achieving uniform stress distribution, albeit without drastically reducing the peak stress levels. The influence of applying a higher-level post-heating scenario (80% laser power) without pre-heating (Case-02) is illustrated clearly in Figure. 22. Similar to the low-level post-heating scenario, the temperature profile exhibits the highest peak temperature (1800 °C) at the deposition endpoint immediately after deposition (0 sec). With high-intensity post-heating, significantly elevated localized temperatures are observed, clearly depicted by pronounced temperature spikes at both ends of the deposited track, corresponding precisely to the four laser scanning passes. The von Mises stress profiles respond accordingly: each laser pass dramatically reduces localized stresses at the respective heating points due to the intense thermal gradients momentarily created as shown in Figure. 23. The significantly higher post-heat temperatures result in notably lower transient stresses at these heated locations compared to the low-intensity scenario. However, upon completion of post-heating, the specimen undergoes rapid cooling, and stresses begin to rise substantially due to solidification-induced contraction as shown in Figure. 24. This increase in residual stress ultimately reaches values comparable to the low-level post-heating scenario. The final stress level achieved upon cooling completion indicates that despite temporary significant stress reductions, the overall magnitude of residual stress does not demonstrate a substantial permanent reduction as shown in Figure. 25.

Additionally, the unclamping stage again slightly reduces stress levels due to elastic relaxation. Thus, while high-level post-heating achieves lower transient stresses during heating, it does not yield a permanent, significant reduction in residual stress after cooling.

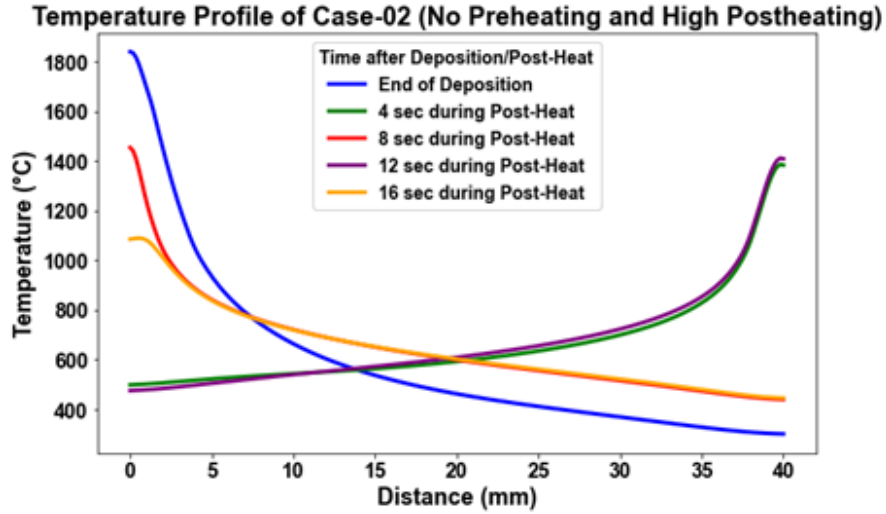


Figure 22. Temperature evolution after low-level (40%) post-heating without pre-heating (Case-01).

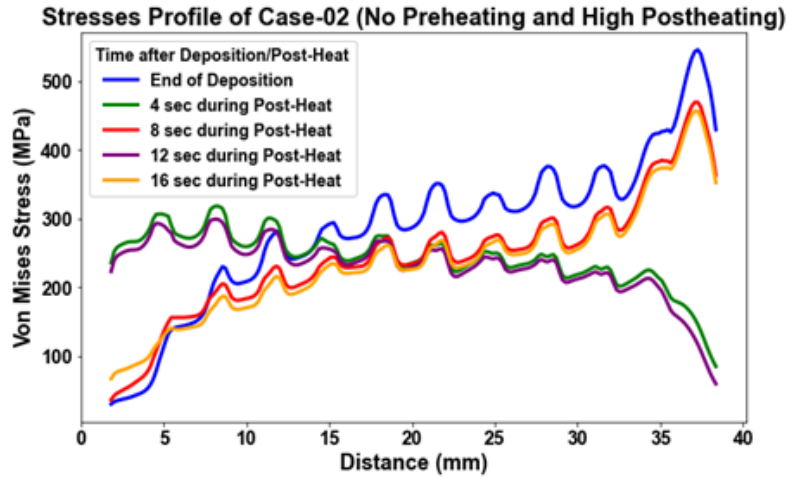


Figure 23. Von-misses evolution after low-level (40%) post-heating without pre-heating (Case-01).

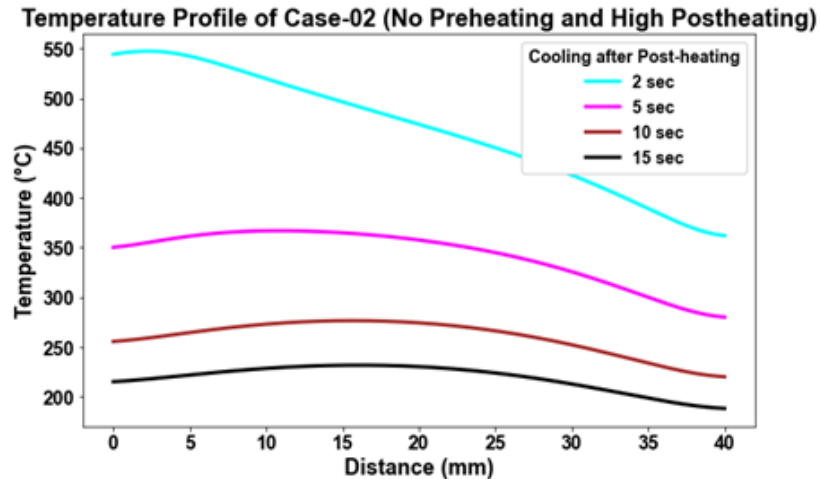


Figure 24. Temperature evolution after low-level (80%) post-heating without pre-heating (Case-01).

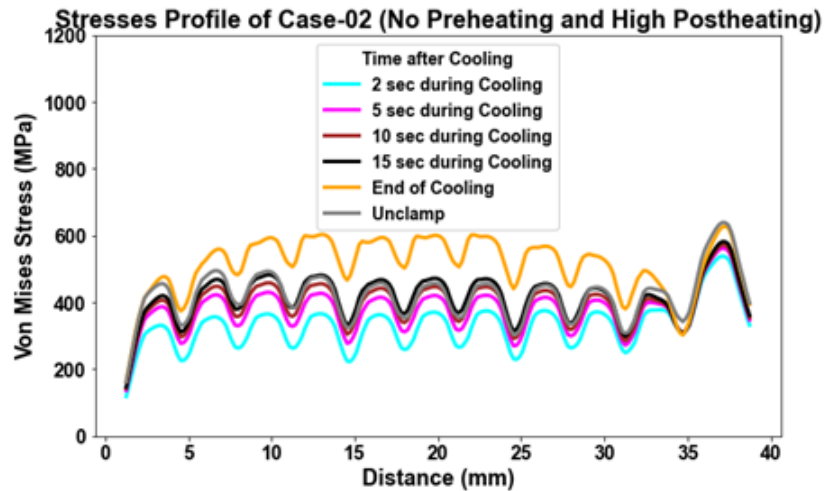


Figure 25. Von-misses evolution after low-level (80%) post-heating without pre-heating (Case-01).

Figures. 26 and 27 compare the temperature and corresponding von Mises stress profiles for scenarios without post-heating, and with low and high post-heating, all conducted without pre-heating. On the temperature profile, the highest temperature immediately after deposition completion is observed in the scenario without post-heating, reflecting rapid cooling from elevated temperatures (1800 °C). The application of low and high post-heating effectively slows the cooling rate, resulting in reduced temperature gradients, especially notable at both ends of the deposited material where the laser initiates its multiple passes, thereby providing more uniform cooling. Despite improved temperature management through post-heating, the von Mises stress profiles show limited overall reduction in residual stresses. A slight decrease in stresses at the endpoints can be observed, attributed to the prolonged presence of the laser at these positions, promoting slower cooling rates and consequently lower thermal gradients. However, the central region of the deposit, experiencing relatively less post-heat exposure, does not exhibit significant stress reduction. This indicates that while post-heating can improve local thermal conditions and marginally reduce endpoint stresses, a substantial overall decrease in residual stress requires a more comprehensive thermal management strategy.

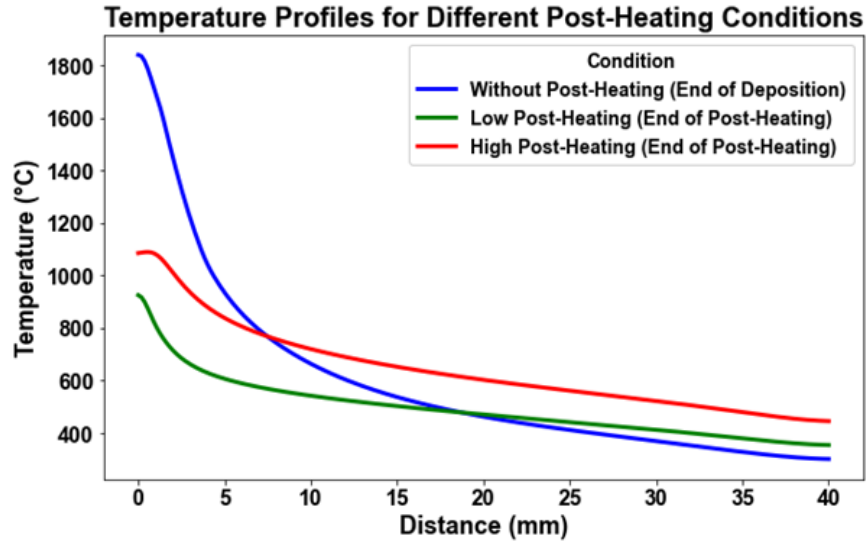


Figure 26. Comparison of temperature profiles for no post-heating, low post-heating (40%), and high post-heating (80%) conditions without pre-heating.

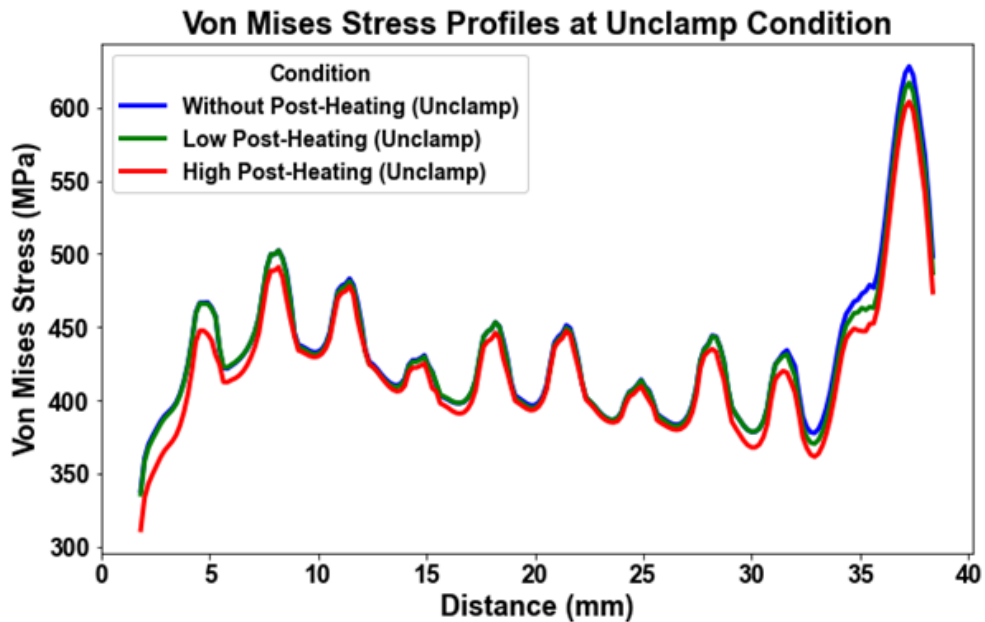


Figure 27. Comparison of von Mises stress profiles for no post-heating, low post-heating (40%), and high post-heating (80%) conditions without pre-heating.

Conclusions

The following key conclusions were drawn from the investigation of pre- and post-heating strategies and their impact on residual stress and temperature distribution in DED processes:

- **Pre-heating Effects:**

- Pre-heating significantly reduced von Mises stresses at the deposition start. High pre-heating (80% laser power) resulted in stresses of approximately 200 MPa, substantially lower than the 325 MPa observed without pre-heating.

- Residual stress magnitudes were strongly correlated with initial substrate temperature gradients; thus, elevated initial temperatures effectively decreased residual stress formation.
- **Post-heating Influence:**
 - Post-heating provided temporary stress relief at the endpoints by maintaining elevated temperatures, thereby delaying solidification-induced stress development.
 - However, once post-heating concluded, temperatures rapidly decreased, and residual stresses reverted to levels comparable with cases without post-heating, indicating limited effectiveness.
- **Stress Evolution during Cooling:**
 - During the final cooling and unclamping stages, stresses at both specimen ends slightly decreased. However, this reduction was minimal relative to the initial preheating-induced stress reduction.
 - This emphasizes pre-heating as a more effective stress mitigation strategy compared to post-heating.

The study highlights the superior effectiveness of pre-heating in managing residual stresses in DED processes, offering valuable insights for optimizing AM practices.

Acknowledgments

The author acknowledges the support of the Intelligent Systems Center (ISC) at Missouri University of Science and Technology for this research.

References

- [1] T. DebRoy, H. L. Wei, J. S. Zuback, T. Mukherjee, J. W. Elmer, J. O. Milewski, A. M. Beese, A. Wilson-Heid, A. De, and W. Zhang, “Additive manufacturing of metallic components – process, structure and properties,” *Progress in Materials Science*, vol. 92, pp. 112–224, 2018.
- [2] F. Wang, “Mechanical properties of additive manufactured ti-6al-4v by electron beam melting,” *Materials Science and Engineering: A*, vol. 740-741, pp. 168–181, 2017.
- [3] E. R. Denlinger, J. C. Heigel, and P. Michaleris, “Residual stress and distortion modeling of electron beam direct manufacturing ti-6al-4v,” *Rapid Prototyping Journal*, vol. 23, no. 3, pp. 375–383, 2017.
- [4] J. P. Kruth, P. Mercelis, J. Van Vaerenbergh, L. Froyen, and M. Rombouts, “Residual stress in selective laser sintering and selective laser melting,” *Proceedings of the Institution of Mechanical Engineers, Part B: Journal of Engineering Manufacture*, vol. 226, no. 6, pp. 980–991, 2012.
- [5] S. H. Chowdhury, K. M. Omer, and R. Kovacevic, “Thermal behavior and mechanical properties of laser metal deposited ti-6al-4v,” *Materials Science and Engineering: A*, vol. 733, pp. 414–430, 2018.
- [6] C. Li, J. Liu, X. Fang, and Y. Guo, “Effect of scan strategy on residual stress and mechanical properties of selective laser melted ti-6al-4v,” *Materials and Design*, vol. 140, pp. 307–315, 2019.

- [7] X. Yao, J. Yin, H. Wang, L. Ke, H. Tang, J. Wang, and W. Zhang, "Laser pre-heating effects on thermal stress and distortion in selective laser melting of ti-6al-4v," *Journal of Materials Processing Technology*, vol. 301, p. 117462, 2022.
- [8] E. R. Denlinger, J. C. Heigel, and P. Michaleris, "Thermal modeling of ti-6al-4v in directed energy deposition using experimental validation," *Additive Manufacturing*, vol. 17, pp. 23–32, 2017.
- [9] X. Lu, X. Lin, M. Chiumenti, M. Cervera, Y. Hu, X. Ji, L. Ma, H. Yang, and W. Huang, "Residual stress and distortion of rectangular and s-shaped ti-6al-4v parts by directed energy deposition: Modelling and experimental calibration," *Additive Manufacturing*, vol. 26, pp. 166–179, 2019.